Supplementary Information: Comparison between First-Principle Calculations and Experimental Studies of XYZ_2 Thermoelectric Compounds

Jan-Hendrik Pöhls,[1] Zhe Luo,[2,3] Umut Aydemir,[3,4] Jon-Paul Sun,[1,5] Shiqiang Hao,[3] Jiangang He,[3] Ian G. Hill,[1,6] Geoffroy Hautier,[7] Anubhav Jain,[8] Xiaoqin Zeng,[2] Chris Wolverton,[3] G. Jeffrey Synder,[3] Hong Zhu,[9,10] Mary Anne White[1,6,11]

Affiliations

1) Department of Physics and Atmospheric Science, Dalhousie University, Halifax, NS B3H 4R2, Canada.
2) National Engineering Research Center of Light Alloy Net Forming, Shanghai Jiao Tong University, Shanghai 200240, PRC.
3) Department of Materials Science and Engineering, Northwestern University, IL 60208, USA.
4) Department of Chemistry, Koc University, Sariyer, Istanbul 34450, Turkey.
5) Department of Mechanical Engineering and Materials Science, Duke University, Durham, NC 27708, USA
6) Clean Technologies Research Institute, Dalhousie University, Halifax, NS B3H 4R2, Canada.
7) Institute of Condensed Matter and Nanosciences (IMCN), Université Catholique de Louvain, Chemin des Étoiles 8, B-1348 Louvain-la-Neuve, Belgium.
8) Energy Technologies Area, Lawrence Berkeley National Lab, 1 Cyclotron Rd, Berkeley, CA, USA.
9) State Key Laboratory of Metal Matrix Composite, Shanghai Jiao Tong University, Shanghai 200240, PRC.
10) University of Michigan - Shanghai Jiao Tong University Joint Institute, Shanghai Jiao Tong University, Shanghai 200240, PRC.
11) Department of Chemistry, Dalhousie University, Halifax, NS B3H 4R2, Canada.

Approximation on the disordered $YCuTe_2$ during phonon calculation

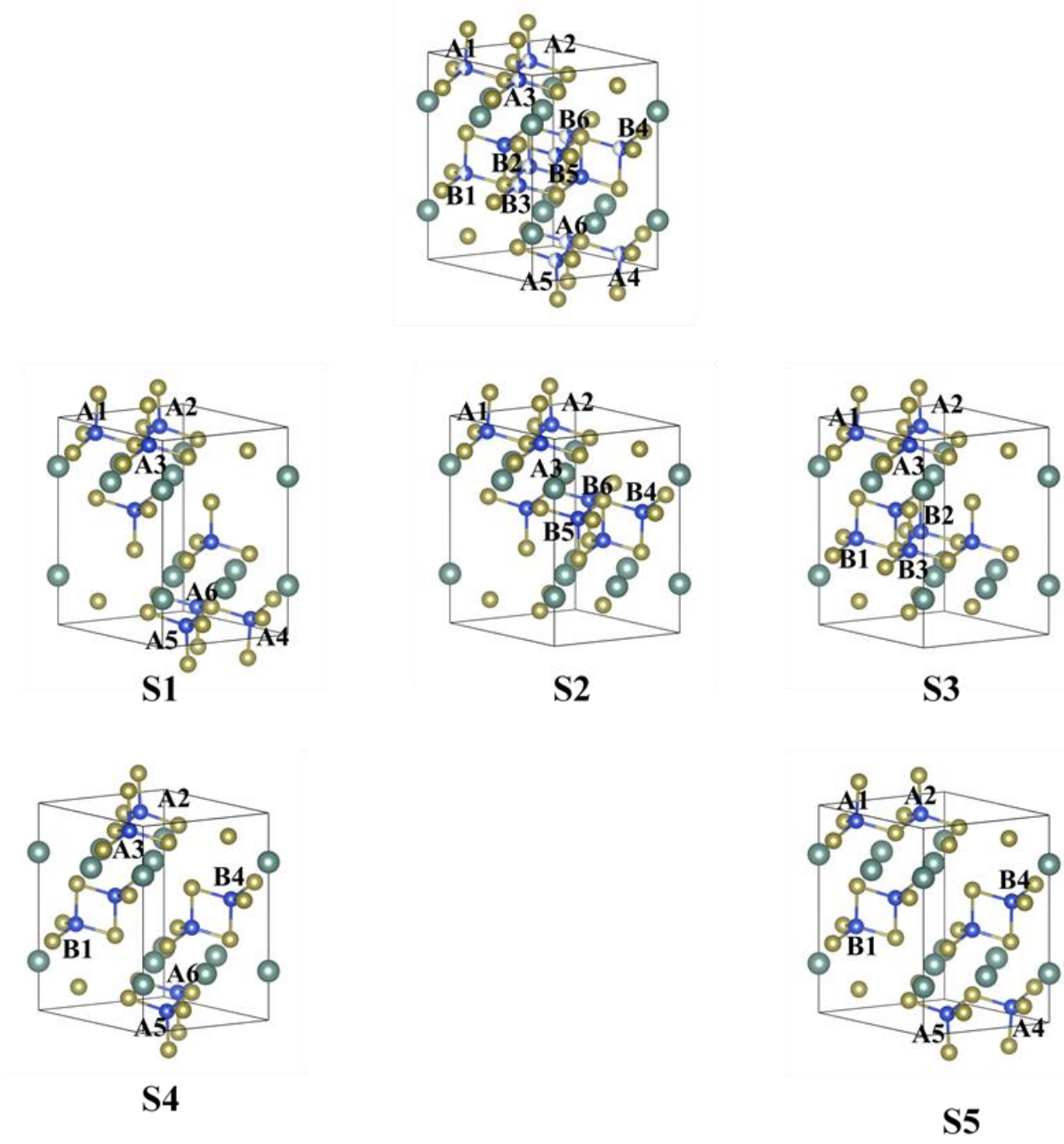

Figure S1: Disorder primitive cell of LT-$YCuTe_2$, in which 2 sets of Wyckoff Cu 6*i* sites are partially occupied, labelled as A1-A6 and B1-B6, respectively. Experimental determined site occupancy factor (SOF) for A is 0.656(7) and B 0.516(7) for LT-$YCu_{1.04}Te_2$. S1-S5 are the approximated stoichiometric ordered structure within the primitive cell. The symmetry was chosen as high as possible during the structure generation to reduce computation cost of the phonon calculations. The green atoms are Y, blue atoms are Cu and yellow Te.

Table S1: Calculated energy of varied models of $YCuTe_2$ in diverse space groups. Lowest energy was found for the space group $C2/m$ which was used for the phonon dispersion curves. The configurations of the site occupancy factor (SOF) are displayed in Figure S1.

	Space Group	SOF		Energy/atom (eV)
		A	B	
S1	$P\bar{3}m1$	1	0	-5.063
S2	$P3m1$	1/2	1/2	-5.047
S3	$P3m1$	1/2	1/2	-5.059
S4	$C2/m$	2/3	1/3	-5.087
S5	$P\bar{1}$	2/3	1/3	-5.084

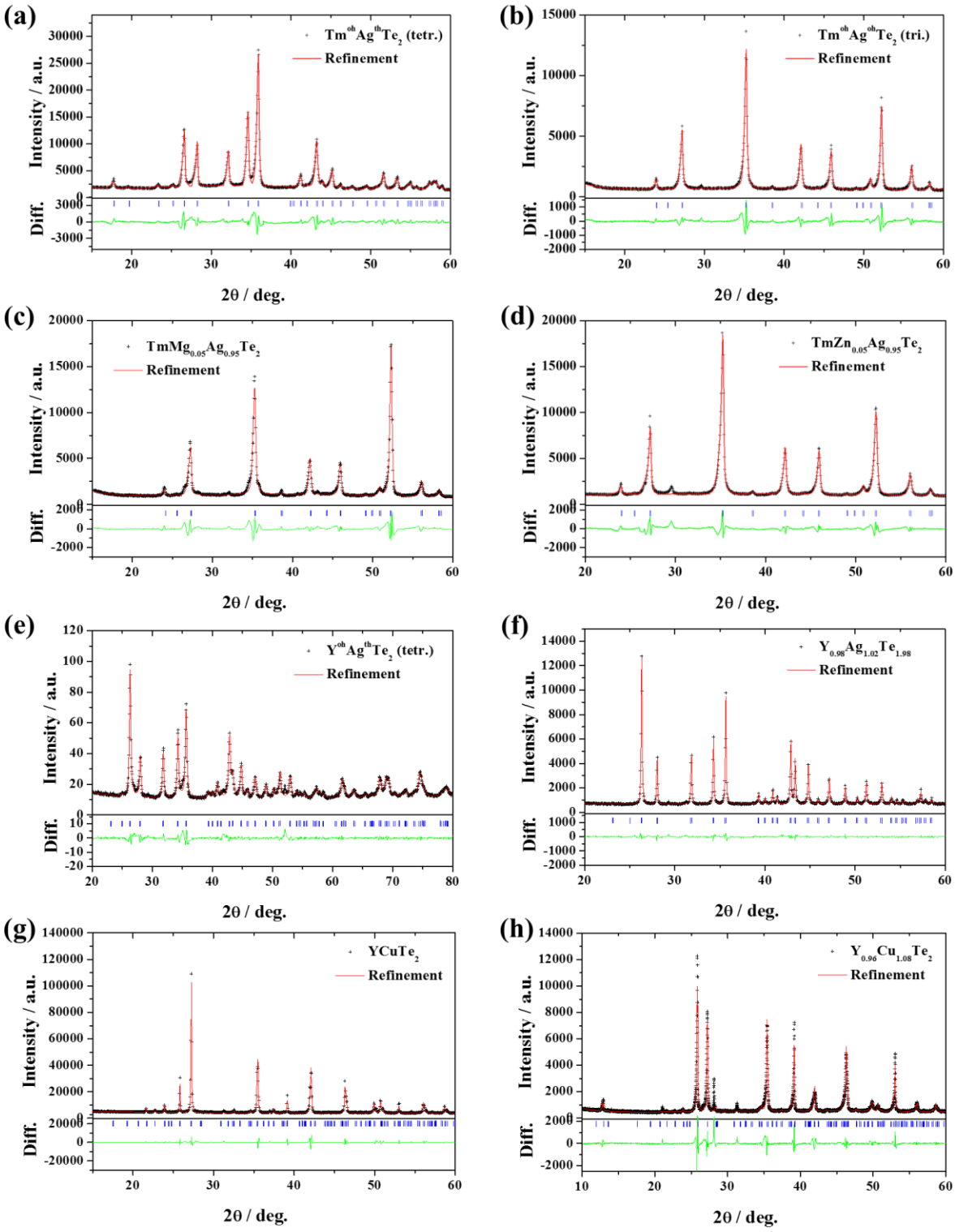

Figure S2: Refined PXRD pattern of (a) LT-$TmAgTe_2$, (b) HT-$TmAgTe_2$, (c) $TmMg_{0.05}Ag_{0.95}Te_2$, (d) $TmMg_{0.05}Ag_{0.95}Te_2$, (e) $YAgTe_2$, (f) $Y_{0.96}Ag_{1.02}Te_{1.98}$, (g) $YCuTe_2$, and (h) $Y_{0.96}Cu_{1.08}Te_2$ using the LeBail method. Blue ticks mark the reflections of the target crystal structure and the green line represents the residual.

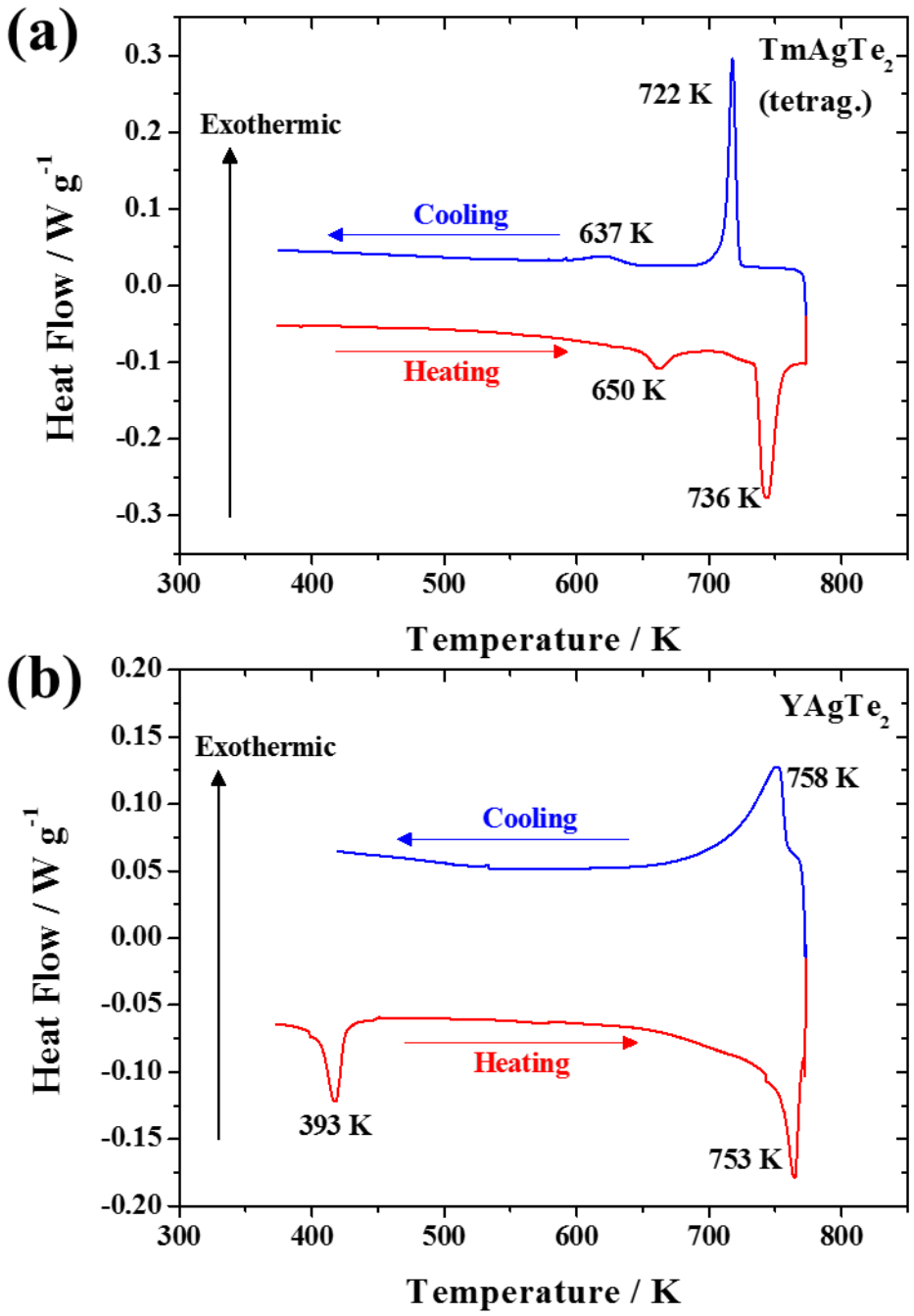

Figure S3: DSC thermograms of (a) $TmAgTe_2$ and (b) $YAgTe_2$. All studied XYZ_2 compounds exhibit reversible phase transitions. Change of enthalpy and change of entropy are given in Table S1.

Table S2: Thermodynamic parameters of $TmAgTe_2$, $YAgTe_2$, and $YCuTe_2$. Onset temperatures, T_{onset}, peak temperature, T_{peak}, change in enthalpy, ΔH, and change in entropy, ΔS, of the phase transitions on heating and cooling. LT peak and HT peak referred to the lower temperature and higher temperature phase transition, respectively.

Compound	T_{onset} / K	T_{peak} / K	ΔH / kJ mol^{-1}	ΔS / J K^{-1} mol^{-1}
Heating				
$TmAgTe_2$ (LT peak)	649.5±1.5	662.1±1.5	1.4±0.1	2.2±0.2
$TmAgTe_2$ (HT peak)	735.6±1.5	743.5±1.5	7.4±0.7	10.1±1.0
$TmAg_{0.95}Zn_{0.05}Te_A$	704.8±1.5	719.1±1.5	0.8±0.1	1.1±0.1
$YAgTe_2$ (LT peak)	393.3±1.5	413.3±1.5	0.6±0.1	0.9±0.1
$YAgTe_2$ (HT peak)	752.7±1.5	765.4±1.5	2.1±0.2	2.8±0.3
$YCuTe_2$	430.2±1.5	440.2±1.5	1.7±0.2	3.9±0.4
$Y_{0.96}Cu_{1.08}Te_2$	340.9±1.5	376.6±1.5	0.4±0.1	1.2±0.1
Cooling				
$TmAgTe_2$ (LT peak)	636.7±1.5	616.5±1.5	0.6±0.1	1.0±0.1
$TmAgTe_2$ (HT peak)	721.8±1.5	717.5±1.5	6.2±0.6	8.6±0.9
$TmAg_{0.95}Zn_{0.05}Te_A$	685.2±1.5	670.1±1.5	1.0±0.1	1.4±0.1
$YAgTe_2$ (LT peak)	400.7±1.5	389.2±1.5	0.8±0.1	2.0±0.2
$YAgTe_2$ (HT peak)	758.1±1.5	751.7±1.5	2.4±0.2	3.2±0.3
$YCuTe_2$	439.2±1.5	434.2±1.5	1.7±0.2	3.9±0.4
$Y_{0.96}Cu_{1.08}Te_2$	392.8±1.5	365.5±1.5	0.5±0.1	1.3±0.1

Table S3: Computed band gap energies using PBE-GGA with and without inclusion of spin-orbit coupling (SOC) and HSE. The LT phases of $TmAgTe_2$ and $YAgTe_2$ were also calculated from the DFT-D3 optimized crystal structure indicating a reduction in band gap energy for non SOC (NSOC). The band gap energies were calculated from a line mesh and unit mesh for GGA and from the unit mesh for HSE06.

DFT	GGA NSOC / eV	GGA SOC / eV	HSE / eV	Exp. / eV
LT-$TmAgTe_2$	0.89-0.90	0.66-0.70	1.73	
HT-$TmAgTe_2$	0.66-0.68	0.38-0.40	1.50	0.54[1]
LT-$YAgTe_2$	0.90-0.92	0.69-0.73	1.58	
LT-$YCuTe_2$	0.51	0.28-0.29	1.37	0.60[2]
HT-$YCuTe_2$	0.57	0.31-0.34	1.47	
DFT-D3				
LT-$TmAgTe_2$	0.73-0.74	0.68-0.69	1.36	
LT-$YAgTe_2$	0.72-0.74	0.67-0.74	1.36	

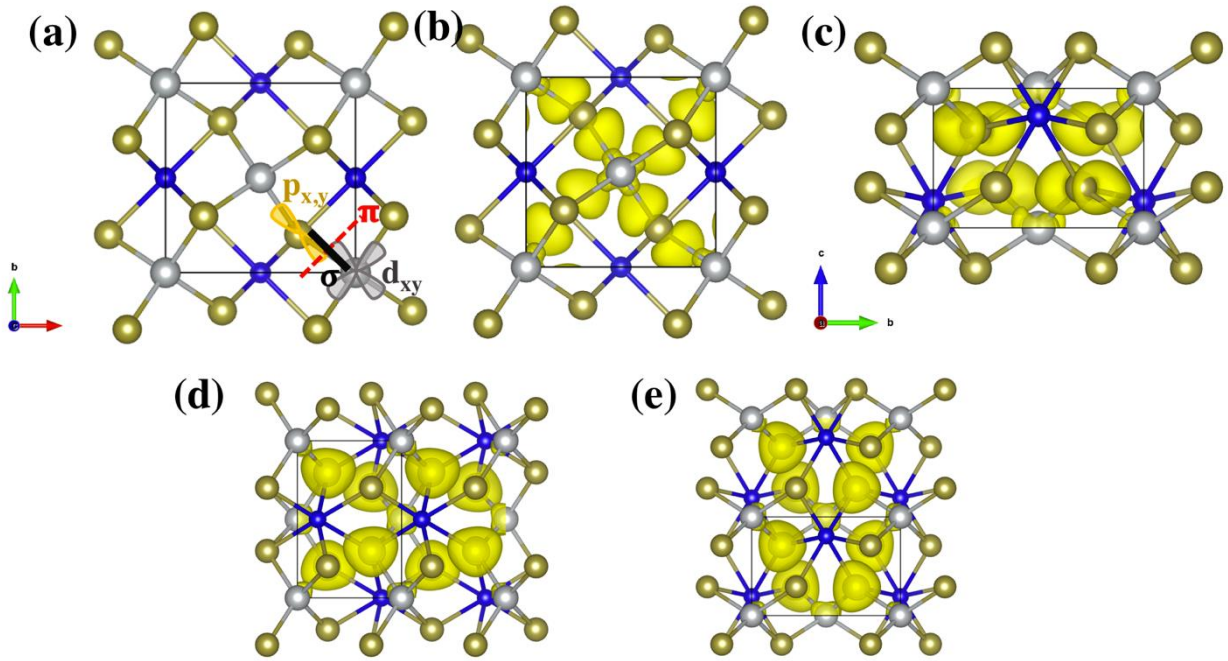

Figure S4: Bonding and anti-bonding orbitals of LT-$TmAgTe_2$. (a) The wave function character of VBM state is the hybridization of the $p_{x,y}$ of Te (yellow) (p_x and p_y are equally contributed), d_{xy} of Ag (silver), and a small fraction of p_z and d_{x2} of Ag (Tm atoms are blue). The dominated $p_{x,y}$ of Te and d_{xy} of Ag are shown. Note that $p_{x,y}$ of Te is parallel to d_{xy} of Ag, but they are not in the same plane. The wave function character of VBM indicates that the bond between $p_{x,y}$ of Te and d_{xy} of Ag should be either a π bond shown by the red dashed line or σ bond by the black solid line. A large partial charge density along the π bond or σ bond implies a bond, while a small or zero charge density implies an anti-bond. (b) Partial charge density (0.003 e/Å^3) of Te-Ag band viewed from *c*-direction; the coexistence of charge near both Te and Ag suggests that energy level of Te $p_{x,y}$ and Ag d_{xy} should be close and rules out the possibility of a non-bond; charge distribution near Te validates the orientation of Te $p_{x,y}$ in (a) rather than the one perpendicular to that in (a); the maximum of the charge density appears near Te, rather than in the middle of Te and Ag, indicating an π anti-bond (c) Partial charge density (0.003 e/Å^3) of Te-Ag band viewed from *a*-direction; the low charge density along the Te-Ag bonds indicates a σ antibond. As results, the VBM should be an anti-bond state, and will move upwards into the band gap with negative stress as indicated by Peng *et al*.[3] (d, e) Partial charge distribution (0.003 e/ Å3) of Te-Tm-Ag band at VBM. Similar to the Te-Ag band at VBM, the hybridization of Te and Ag in Te-Tm-Ag behaves like an anti-bonding state. However, although the isosurface of the charge density is missing at Tm, the orbits of Tm still participate in the hybridization and the isosurface stretches along the Te-Tm bonds, which indicates that the Te-Tm bond in Te-Tm-Ag should be ionic bonding states. As result, the Te-Tm-Ag band near the VBM should be a mixing of anti-bonding states of Te-Ag and ionic bonding states of Te-Tm. The latter states should be repulsive and increase the band gap with negative stress.

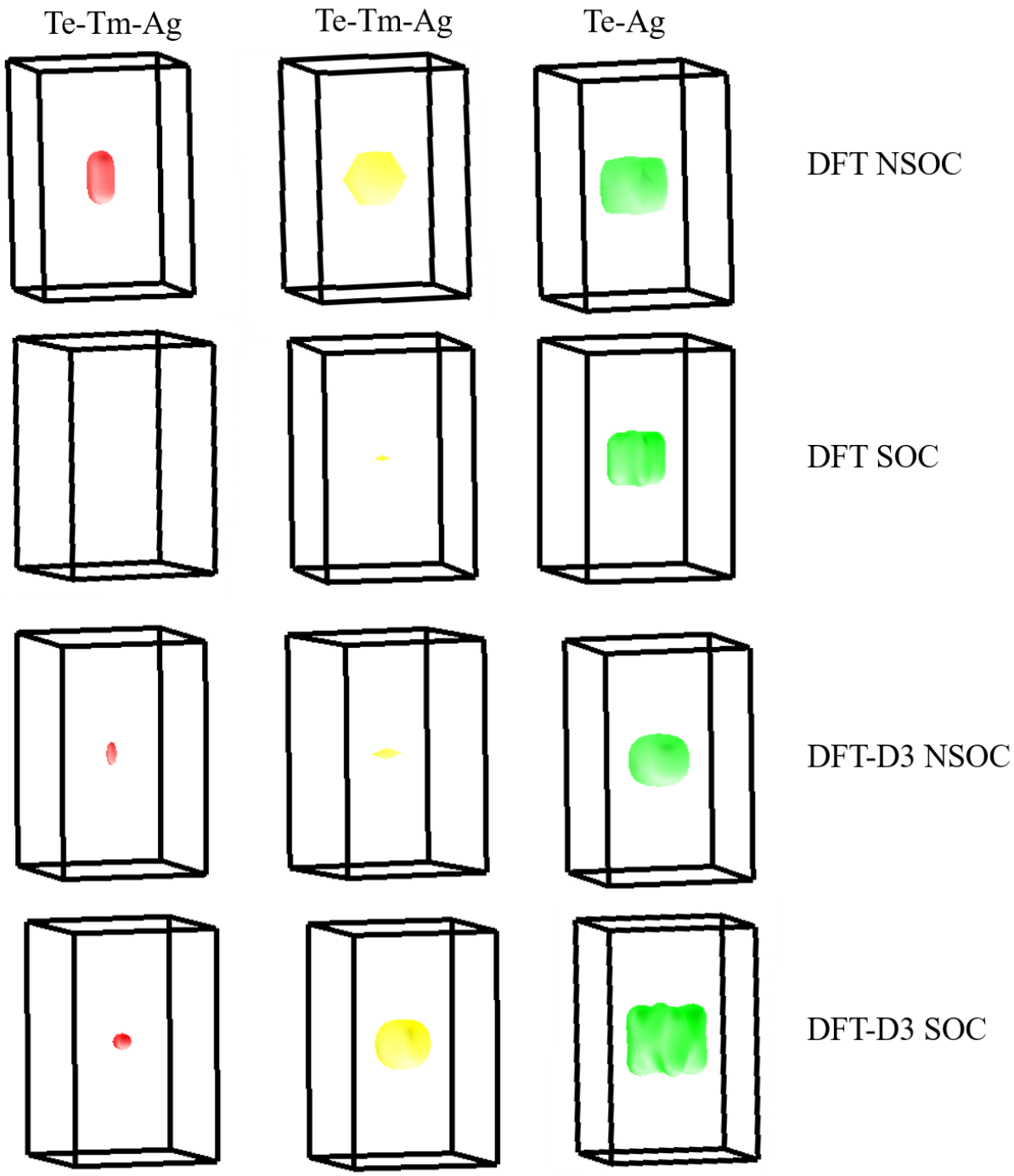

Figure S5: Fermi surfaces of the two Te-Tm-Ag and Te-Ag valence bands of LT-$TmAgTe_2$ at an energy of E-E_F = -0.3 eV. All three valence bands are nearly degenerate if DFT NSOC was applied. With the inclusion of SOC, the two degenerate Te-Tm-Ag bands splits in both cases (DFT and DFT-D3). Furthermore, the inclusion of DFT-D3 leads to a larger split of the Te-Tm-Ag and Te-Ag bands compared to DFT NSOC.

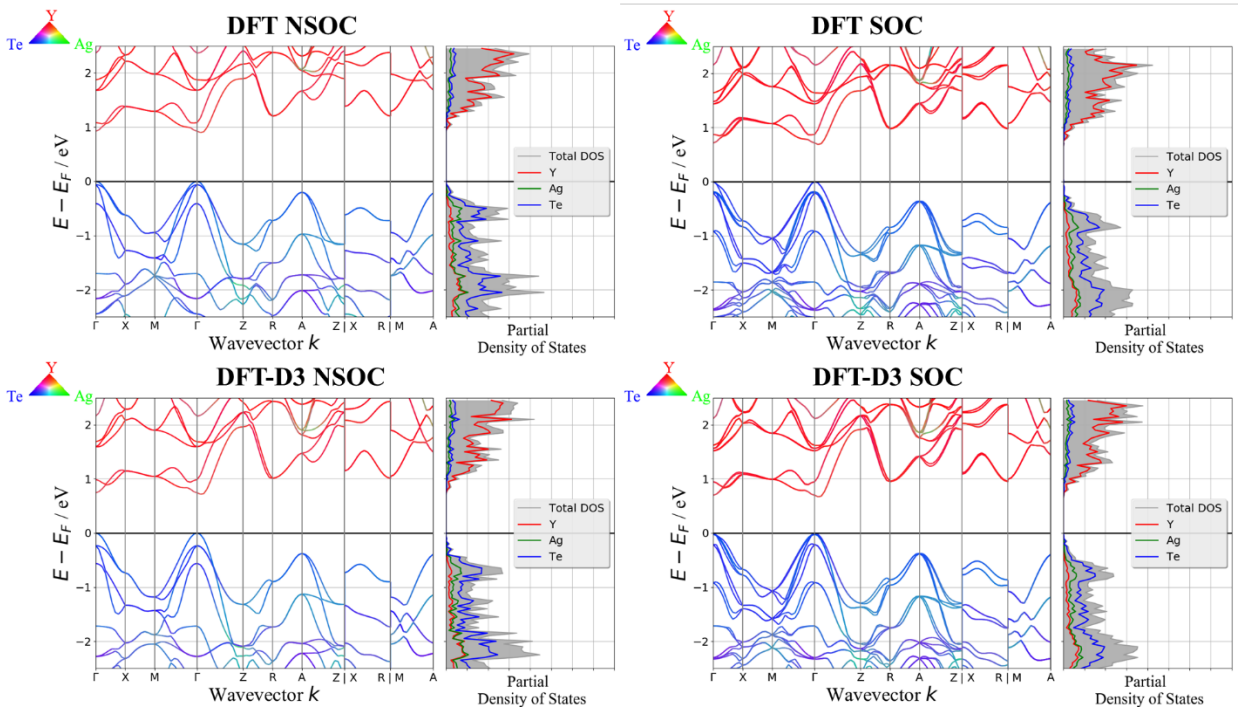

Figure S6: Electronic band structures of LT-$YAgTe_2$ using PBE-GGA with (SOC) and without (NSOC) the inclusion of spin-orbit coupling and van der Waals interactions (DFT-D3). Similar to $TmAgTe_2$, the degeneracy of the valence bands breaks with inclusion of SOC and/or DFT-D3. The colors in the electronic band structure represent the contributions of the elements onto the various band structures.

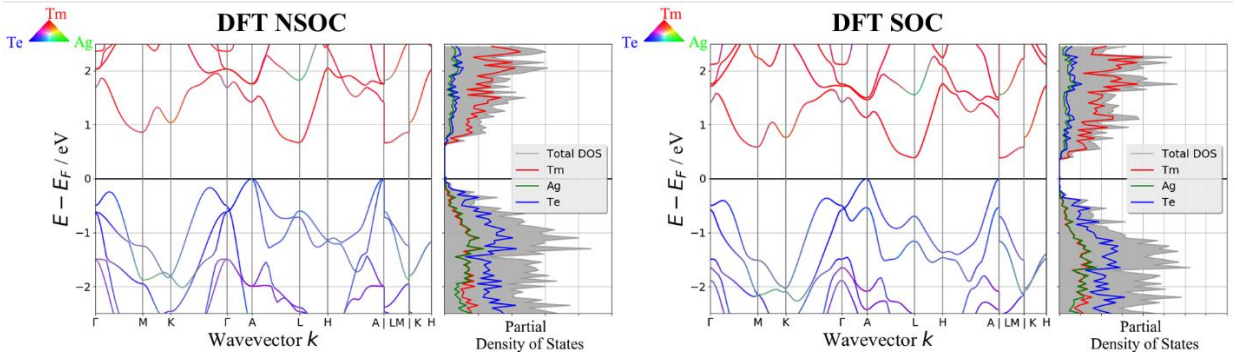

Figure S7: Electronic band structure of HT-$TmAgTe_2$ using PBE-GGA with (SOC) and without (NSOC) the inclusion of spin-orbit coupling (SOC). The band gap and the degeneracy of the valence bands reduce with the inclusion of SOC. The colors in the electronic band structure represent the contributions of the elements onto the various band structures.

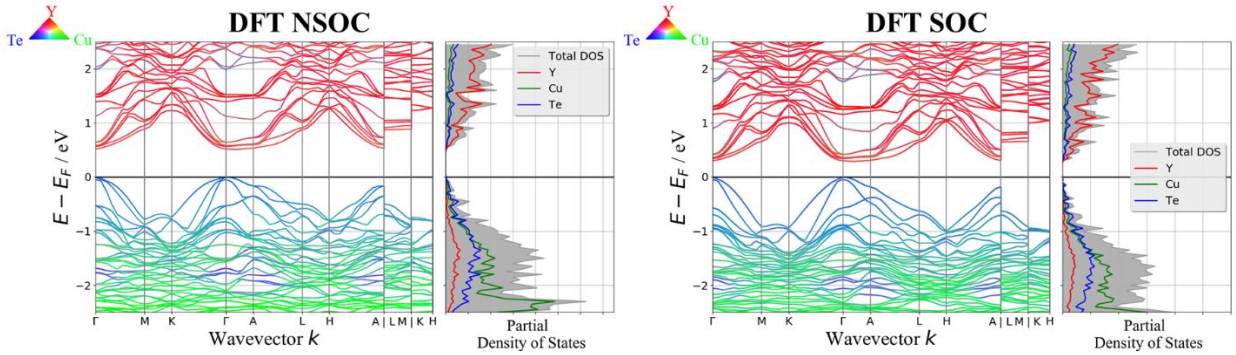

Figure S8: Electronic band structure of LT-$YCuTe_2$ using PBE-GGA with (SOC) and without (NSOC) the inclusion of spin-orbit coupling (SOC). The discrepancy at the valence band maximum between the NSOC and SOC band structures is less significant for the Cu-based compounds than for the Ag-based compounds. The colors in the electronic band structure represent the contributions of the elements onto the various band structures.

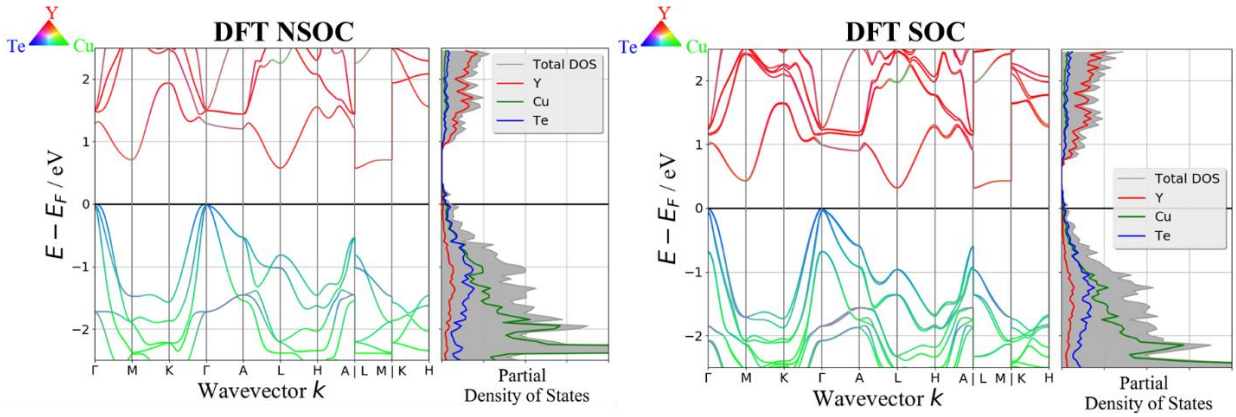

Figure S9: Electronic band structure of HT-$YCuTe_2$ using PBE-GGA with (SOC) and without (NSOC) the inclusion of spin-orbit coupling (SOC). In contrast to the LT-phase, the valence bands are more curved reducing the band effective mass and hence, increasing the electrical conductivity. The colors in the electronic band structure represent the contributions of the elements onto the various band structures.

Table S4: Average relative deviation of the computed electrical resistivity over temperature using different methods (including SOC and DFT-D3) to the experimental values. Minimum and maximum relative deviation are given to achieve a better understanding of the accuracy of the method.

Compound	Computational Method	Average relative deviation / %	Minimum relative deviation / %	Maximum relative deviation /%
LT-$TmAgTe_2$	DFT PBE-NSOC	25.5	8.0	43.5
	DFT PBE-SOC	8.3	0.1	32.3
	DFT HSE-NSOC	25.7	8.0	43.6
	DFT-D3 PBE-NSOC	8.8	0.6	24.5
	DFT-D3 PBE-SOC	8.4	0.2	23.6
	DFT-D3 HSE-NSOC	9.6	0.1	23.9
HT-$TmAgTe_2$	DFT PBE-NSOC	73.2	5.4	173.2
	DFT PBE-SOC	24.5	0.9	64.4
	DFT HSE-NSOC	93.5	5.4	340.3
$YAgTe_2$	DFT PBE-NSOC	66.8	6.6	210.2
	DFT PBE-SOC	58.2	2.2	137.4
	DFT HSE-NSOC	67.0	6.5	212.1
	DFT-D3 PBE-NSOC	58.2	2.2	142.3
	DFT-D3 PBE-SOC	56.5	0.4	129.7
	DFT-D3 HSE-NSOC	59.4	1.2	154.2
LT-$YCuTe_2$	DFT PBE-NSOC	32.1	0.9	90.9
	DFT PBE-SOC	31.1	0.5	54.3
	DFT HSE-NSOC	31.1	1.5	91.5
HT-$YCuTe_2$	DFT PBE-NSOC	30.6	2.5	92.0
	DFT PBE-SOC	23.6	3.4	44.2
	DFT HSE-NSOC	30.7	2.2	92.9

Table S5: Average relative deviation of the computed Seebeck coefficient over temperature using different methods (including SOC and DFT-D3) to the experimental values. Minimum and maximum relative deviation are given to achieve a better understanding of the accuracy of the method.

Compound	Computational Method	Average relative deviation / %	Minimum relative deviation / %	Maximum relative deviation /%
LT-$TmAgTe_2$	DFT PBE-NSOC	1.8	0.0	7.4
	DFT PBE-SOC	18.5	16.4	22.4
	DFT HSE-NSOC	1.8	0.0	7.4
	DFT-D3 PBE-NSOC	15.5	12.9	20.7
	DFT-D3 PBE-SOC	8.4	6.8	11.7
	DFT-D3 HSE-NSOC	15.6	13.1	20.8
HT-$TmAgTe_2$	DFT PBE-NSOC	13.2	0.4	44.0
	DFT PBE-SOC	38.4	7.9	78.7
	DFT HSE-NSOC	16.1	0.5	44.4
$YAgTe_2$	DFT PBE-NSOC	95.3	22.9	180.9
	DFT PBE-SOC	59.6	2.4	121.5
	DFT HSE-NSOC	95.2	22.7	180.6
	DFT-D3 PBE-NSOC	59.8	0.1	122.6
	DFT-D3 PBE-SOC	77.2	15.5	154.9
	DFT-D3 HSE-NSOC	60.5	0.1	122.6
LT-$YCuTe_2$	DFT PBE-NSOC	22.1	1.7	35.7
	DFT PBE-SOC	23.6	3.8	50.6
	DFT HSE-NSOC	24.8	12.0	35.6
HT-$YCuTe_2$	DFT PBE-NSOC	31.3	10.4	55.8
	DFT PBE-SOC	11.0	0.1	29.5
	DFT HSE-NSOC	31.9	12.6	56.1

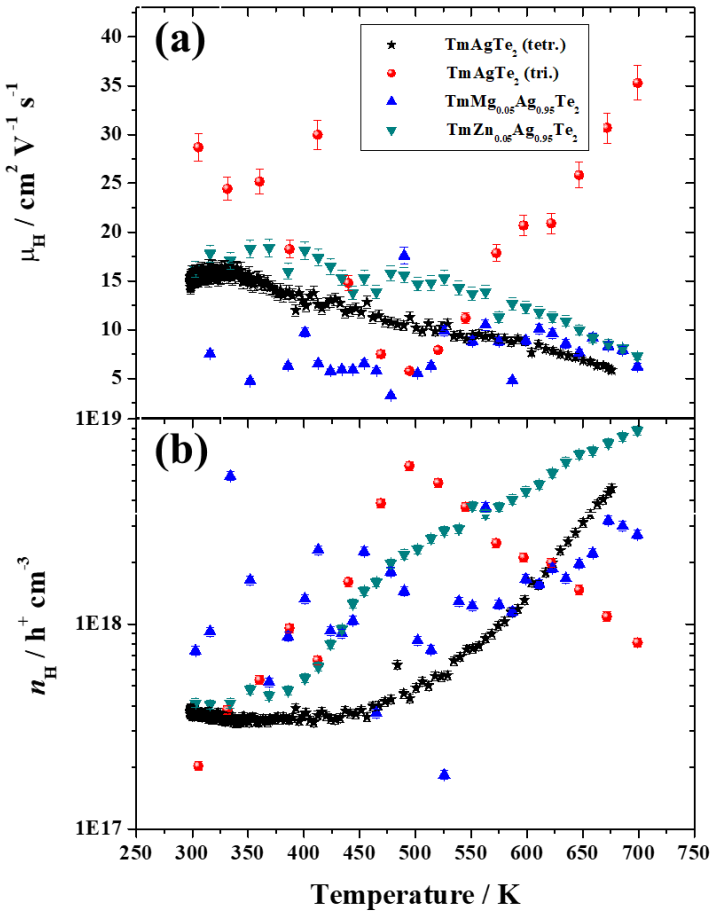

Figure S10: Hall mobility, μ_H, and Hall carrier concentration, n_H, of $TmAgTe_2$ compounds. An increase in hole carrier concentration was observed for the Zn-doped sample.

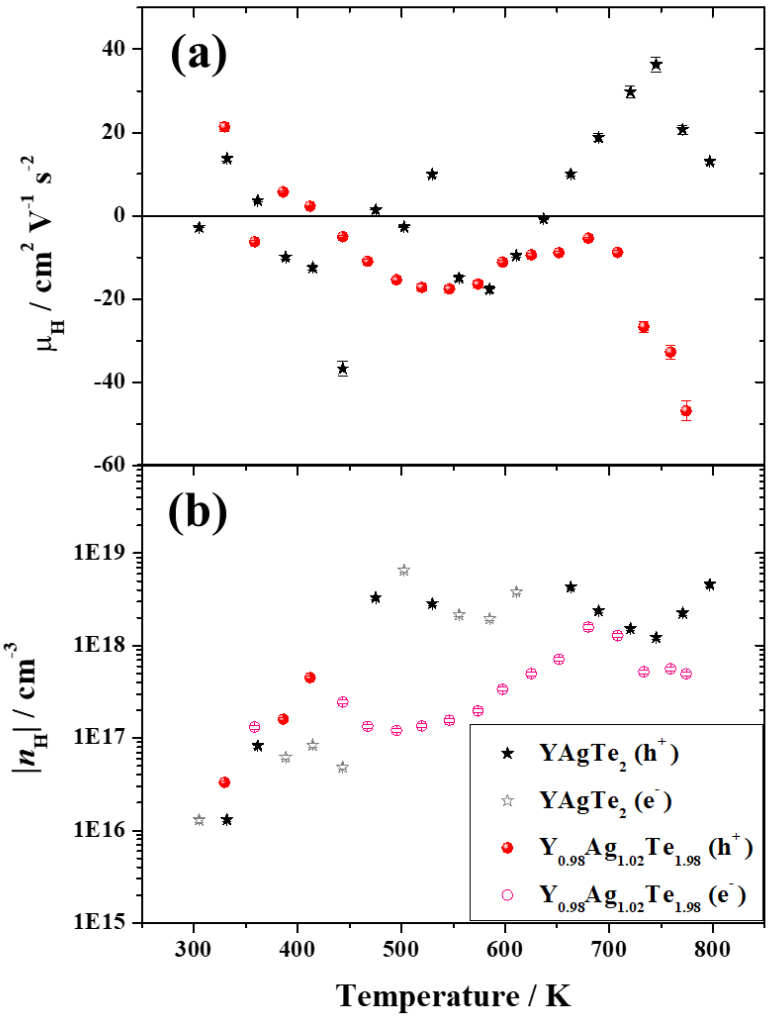

Figure S11: Hall mobility, μ_H, and Hall carrier concentration, n_H, of $YAgTe_2$ compounds. The Hall coefficient switched from positive to negative, however, the Seebeck coefficient suggests that $YAgTe_2$ is *p*-type. Note that the Hall coefficient changed from positive to negative most likely due to high contact resistance. For the carrier concentration, the absolute value of n_H was taken resulting in a continuous curve.

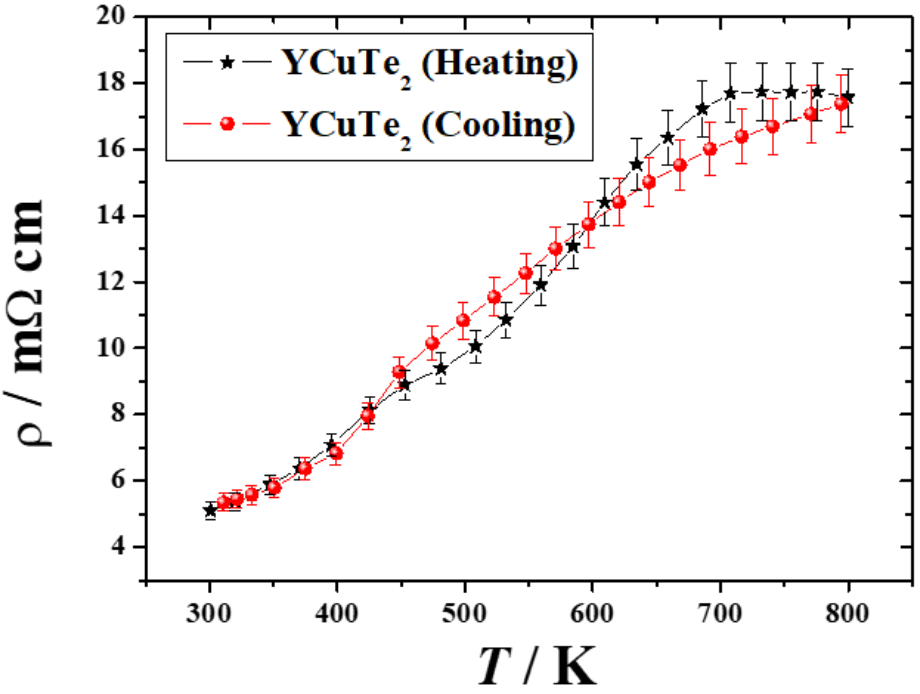

Figure S12: Electrical resistivity of $YCuTe_2$ on heating and cooling. The electrical resistivity of both curves is in uncertainties.

Table S6: Computed Debye temperatures from phonon dispersion curves for LT-$TmAgTe_2$, HT-$TmAgTe_2$, $YAgTe_2$, and $YCuTe_2$.

Compound	Debye temperature, θ_D / K
LT-$TmAgTe_2$	150 (with DFT-D3)
HT-$TmAgTe_2$	126 (with DFT-D3)
$YAgTe_2$	107 (with DFT-D3)
	125 (without DFT-D3)
$YCuTe_2$	172 (without DFT-D3)

Table S7: Experimental average coefficient of linear expansion of $TmAgTe_2$, $YAgTe_2$, and $YCuTe_2$ on heating (H) and cooling (C). Additionally, the coefficient of volumetric expansion was computed indicating a slightly lower expansion.

Compound	Temperature Range (H) / K	α (H, experiment) / 10^{-6} K^{-1}	Temperature Range (C) / K	α (C, experiment) / 10^{-6} K^{-1}	α_V (computed) / 10^{-6} K^{-1}
$TmAgTe_2$	350-675	19±2	350-625	20±2	39-45
$YAgTe_2$	525-595	0±2	425-550	13±2	41-46
$YCuTe_2$	450-675	27±2	450-675	27±2	

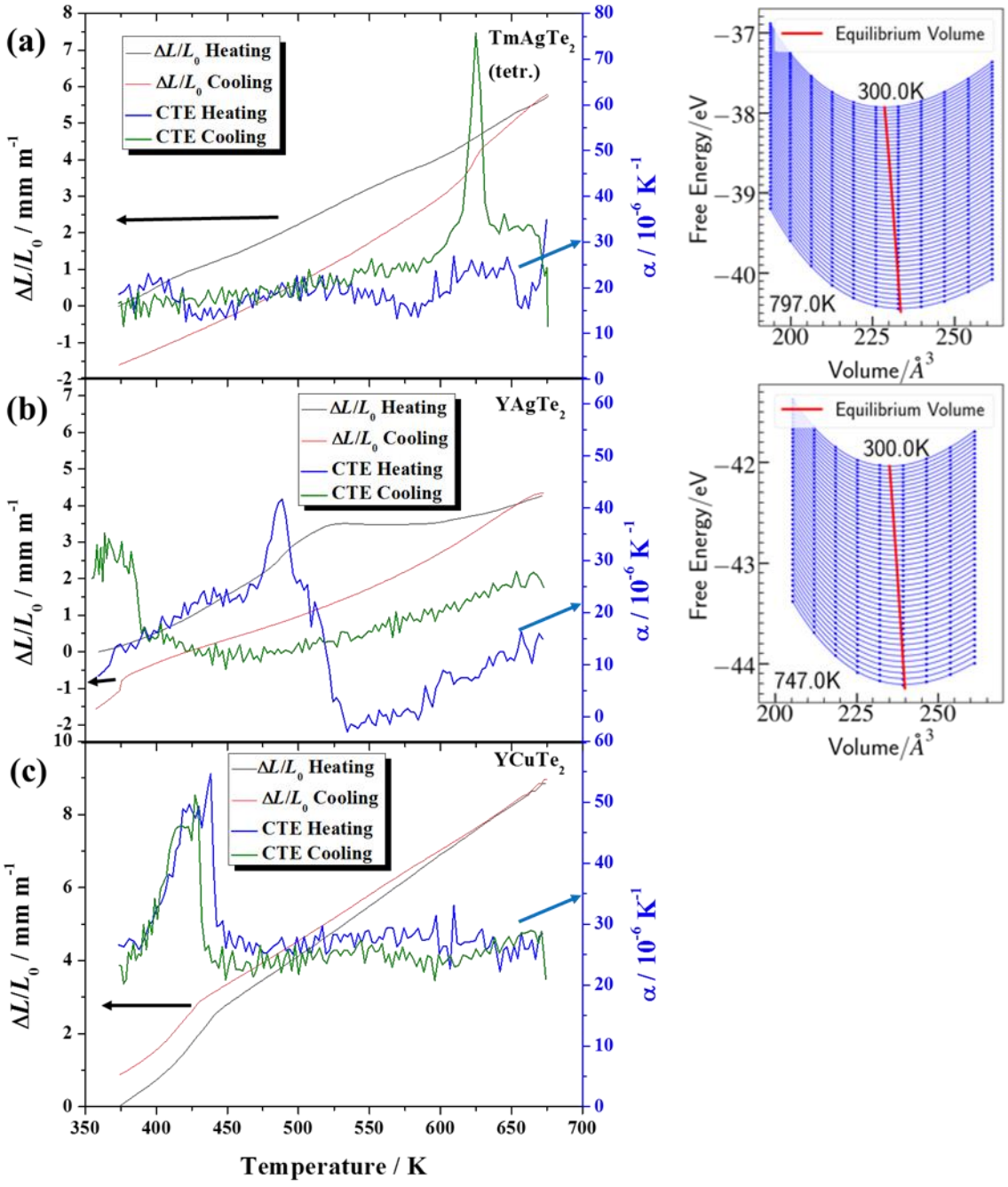

Figure S13: Strain and coefficient of linear expansion, α, of (a) $TmAgTe_2$, (b) $YAgTe_2$, and (c) $YCuTe_2$. Whereas the coefficient of linear expansion for $TmAgTe_2$ and $YCuTe_2$ is constant over a wide temperature range, the coefficient of linear expansion for $YAgTe_2$ changes constantly suggesting a mix phase. The computed free energy diagrams to calculate the theoretical coefficient of volumetric expansion indicate an increase in volume with temperature. Due to the large supercell of disordered $YCuTe_2$, the computational cost was too expensive and is beyond scope of the present study.

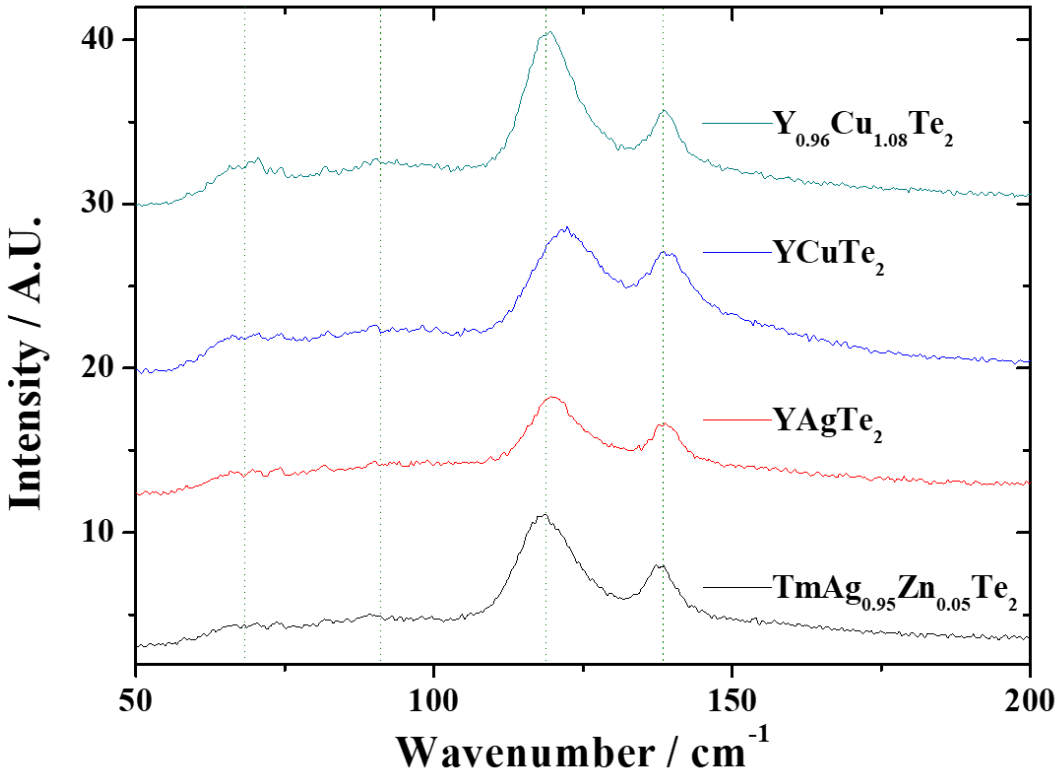

Figure S14: Raman spectra of $Y_{0.96}Cu_{1.08}Te_2$, $YCuTe_2$, $YAgTe_2$, and $TmAg_{0.95}Zn_{0.05}Te_2$. Slightly higher frequencies were observed for $YCuTe_2$ which is consistent with phonon DOS.

Table S8: Computed thermoelectric figures of merit at 600 K calculated from PBE-GGA band structures with and without inclusion of spin orbit coupling (SOC) and HSE. The LT phases of $TmAgTe_2$ and $YAgTe_2$ were also calculated from the DFT-D3 optimized crystal structure. The lattice thermal conductivity was predicted using the Cahill-Pohl model and the computed elastic properties.

DFT	GGA NSOC	GGA SOC	HSE	Exp.
LT-$TmAgTe_2$	0.067	0.057	0.066	0.056±0.011
HT-$TmAgTe_2$	0.137	0.046	0.142	0.277±0.055
LT-$YAgTe_2$	0.233	0.181	0.233	0.021±0.004
LT-$YCuTe_2$	0.684	0.234	0.729	0.414±0.083
HT-$YCuTe_2$	0.808	0.449	0.815	0.414±0.083
DFT-D3				
LT-$TmAgTe_2$	0.056	0.065	0.055	0.056±0.011
LT-$YAgTe_2$	0.175	0.218	0.175	0.021±0.004

Table S9: Conductive effective mass of HT-$TmAgTe_2$ at 650 K determined from computed band structures using different exchange-correlation functionals and SOC, and BoltzTrap. Two different carrier concentrations were used indicating that the conductive effective mass increases with carrier concentration.

Band gap	SOC	Conductive effective mass / m_0	
		$2.5 \cdot 10^{18}$ h^+ cm^{-3}	$2.5 \cdot 10^{19}$ h^+ cm^{-3}
PBE	SOC	0.217	0.400
PBE	NSOC	0.351	0.366
HSE	NSOC	0.375	0.402

References

[1] H. Zhu, G. Hautier, U. Aydemir, Z. M. Gibbs, G. Li, S. Bajaj, J.-H. Pöhls, D. Broberg, W. Chen, A. Jain, M. A. White, M. Asta, G. J. Snyder, K. Persson, G. Ceder, *J. Mater. Chem. C* **2015**, *3*, 10554–10565.

[2] U. Aydemir, J.-H. Pöhls, H. Zhu, G. Hautier, S. Bajaj, Z. M. Gibbs, W. Chen, G. Li, S. Ohno, D. Broberg, S. D. Kang, M. Asta, G. Ceder, M. A. White, K. Persson, A. Jain, G. J. Snyder, *J. Mater. Chem. A* **2016**, *4*, 2461–2472.

[3] X. Peng, Q. Wei, A. Copple, *Phys. Rev. B* **2014**, *90*, 085402.